Calibrating Mixing-length Theory for Thermal Convection in Rocky Planets

F. W. Wagner[1]⋆, A.-C. Plesa[2], and A. B. Rozel[1]

[1] *Institute of Geophysics, ETH Zurich, Sonneggstrasse 5, 8092 Zurich, Switzerland*

[2] *Institute of Planetary Research, DLR Berlin-Adlershof, Rutherfordstrasse 2, 12489 Berlin, Germany*

SUMMARY

We present a calibration of the mixing-length parameter in the local mixing-length theory used to model thermal convection inside rocky planets. The parameterization is derived from a comparison of three-dimensional (3-D) numerical simulation experiments to predictions by the one-dimensional (1-D) mixing-length theory with a depth-dependent mixing length. The comparison encompasses a wide variety of parameters, i.e., Rayleigh numbers ranging from 10^4 to 10^{10} and viscosity contrasts up to 10^6 have been investigated for a convective system heated either solely from below or from both below and within. We find that the mixing length is sensitive to both viscosity contrast and Rayleigh number. With the commonly used scaling relationship, mixing-length theory is unable to reproduce simultaneously heat flux and temperature of the numerical simulation experiments with satisfactory accuracy. According to the calibration, we identify that the mixing length depends on the convection regime. In particular, stagnant-lid convection should be separated from sluggish-lid and mobile-lid convection. In the mobile-lid regime, the mixing length is generally much larger than in the stagnant-lid regime. The presented parameterization yields thermal profiles in excellent agreement with those obtained from fully dynamic convection simulations and important physical properties such as surface heat flux and average mantle temperature can be computed with small errors. This establishes the mixing-length theory as a viable alternative to other parameterized con-

vection models including the widely used boundary-layer theory and offers the possibility to study the thermal state of a large number of Earth-like planets.

Key words: mixing-length theory, mixing-length calibration, mantle convection, terrestrial planets, Nusselt number, average temperature

1   INTRODUCTION

The internal dynamics and thermal evolution of terrestrial planets is mainly governed by the efficiency of convective heat transport through the viscous mantle (Schubert et al. 2001). Since it is computationally challenging to investigate a large parameter space while precisely modeling the full convective heat flux, parameterized descriptions of thermal convection are essential. A simple method to quickly calculate the convective heat transport is known as the mixing-length theory (MLT).

MLT was originally developed by Taylor (1915) and Prandtl (1925) in the early 20th century. The basic idea behind this theory is that heat is transported by thermal parcels over characteristic length scales before dispersing into the surrounding fluid. The velocity of such parcels can then be related to the local temperature gradient from which convective heat flux and temperature distribution is obtained. Today, mixing-length formulations are frequently used to numerically model turbulent and convective motions in the atmospheric boundary layer (Priestley 1959; Holton & Hakim 2013) or to estimate the convective energy transport within turbulent convecting stellar interiors (Vitense 1953; Hansen et al. 2004).

Originally derived solely for fluids characterized by the combination of low Prandtl and high Rayleigh numbers, Sasaki & Nakazawa (1986) extended the mixing-length theory by reformulating it for highly viscous fluids corresponding to low Reynolds numbers. The extension is based on the estimation of vertical velocity by considering the balance between the buoyancy force operating on the thermal parcel and the viscous drag instead of the free-fall velocity. Abe (1995) later

---

⋆ frank.wagner@erdw.ethz.ch

proposed the first parameterization of the depth-dependent mixing length actually applicable for planetary mantles possessing top and bottom boundary layers.

A report assessing the efficiency of heat transport according to the mixing-length theory demonstrated that the method can be used to calculate the radially averaged distribution of temperature across a convective layer with strongly temperature-dependent viscosity (Yamagishi & Yanagisawa 2001-2002). Subsequently, a study carried out by Tachinami et al. (2011) compared the mixing-length theory with conventional parameterized convection models (Sharpe & Peltier 1979) and the commonly used boundary-layer theory (Stevenson et al. 1983); they found that all three methods agree reasonably well for viscosity contrasts up to 10^4. However, a detailed comparison between sophisticated convection experiments and the mixing-length theory has not yet been conducted. Furthermore, a highly variable viscosity and/or changes in how the fluid is heated drastically influence convection pattern and separate scaling laws are required (Solomatov 1995). Unfortunately, no systematic study describing such effects with respect to MLT is currently available.

Abe (1997) originally deployed the mixing-length theory to study the thermal and chemical evolution of Earth's global magma ocean during planet formation. Since then, MLT has occasionally been used in the context of planetary science, e.g., to model the thermal evolution of early Mars (Senshu et al. 2002), to investigate the metallic core and tectonic history of Jovian icy satellites (Kimura et al. 2007; Kimura et al. 2009), and more recently to compute the interior structure and thermal evolution of Saturnian icy satellites (Sohl et al. 2014; Kamata 2018). Furthermore, Tachinami et al. (2011) used this method to assess the lifetime of self-generated magnetic fields of Earth-like planets beyond the Solar System, while Wagner et al. (2011; 2012) applied such a formulation to calculate the thermal state of the first rocky exoplanets.

In the present study, the extension of the mixing-length theory to highly viscous fluids is systematically reviewed. For this purpose, we conduct a wide variety of experiments with the mantle convection code Gaia (Hüttig & Stemmer 2008; Hüttig et al. 2013). These numerical experiments cover Rayleigh numbers from 10^4 to 10^{10} and viscosity contrasts up to 10^6 across a convecting fluid heated either solely from below or from both below and within a spherical shell. We then

calibrate the mixing-length parameter in the local mixing-length theory to accurately reproduce the distributions of heat flux and temperature in three-dimensional (3-D) convection models. This calibration is performed at the statistical steady-state stage for the fluid dynamic problem and at steady state for the 1-D MLT model. Finally, it is demonstrated that the proposed calibration makes the mixing-length approach an efficient and reliable tool to model the thermal state of planetary interiors.

2   METHOD

2.1   Mixing Length

We consider the two standard convective heat transfer mechanisms: (a) conduction, where heat is transmitted through lattice vibrations in crystals and (b) advection, where heat is transported by matter in a fluid-like manner. Within the framework of mixing-length theory, these two mechanisms can be separated by comparing the local to adiabatic temperature gradient. Convective regions are then defined as layers for which the former gradient exceeds the latter. In the following, we describe in detail how heat transfer is modeled with respect to the mixing-length formalism.

We begin with the advection-diffusion equation of a convecting fluid (Poirier 2000; Gerya 2010):

$$\rho C_{\mathrm{P}} \frac{\partial T}{\partial t} = \rho C_{\mathrm{P}} \boldsymbol{v} \cdot (\boldsymbol{\nabla} T_{\mathrm{S}} - \boldsymbol{\nabla} T) + \boldsymbol{\nabla} \cdot (k_{\mathrm{c}} \boldsymbol{\nabla} T) + \rho H, \tag{1}$$

where ρ is the density, C_{P} is the specific heat capacity, T is the temperature, t denotes the time, $\boldsymbol{v}$ refers to the velocity field, k_{c} is the thermal conductivity, and H is a specific heat production rate. The subscript S indicates an adiabatic process, thus explicitly distinguishes between adiabatic and local temperature. Equation [1] describes the balance of thermal energy in a continuum and relates temperature changes due to the advective and conductive heat transport, as well as the generation of internal heat.

Reformulating Eq. [1] in terms of the heat flux $\boldsymbol{q}$ yields

$$\rho C_{\mathrm{P}} \frac{\partial T}{\partial t} = -\boldsymbol{\nabla} \cdot \boldsymbol{q} + \rho H, \tag{2}$$

where $\boldsymbol{q}$ is the sum of advective and conductive heat fluxes. The conductive heat flux $\boldsymbol{q}_{\mathrm{cond}}$ can be

obtained from Fourier's law

$$\boldsymbol{q}_{\mathrm{cond}} = -k_{\mathrm{c}}\boldsymbol{\nabla}T. \tag{3}$$

To evaluate the advective heat flux, we use the mixing-length approach. According to MLT, the advective heat flux $\boldsymbol{q}_{\mathrm{adv}}$ can be expressed as

$$\boldsymbol{q}_{\mathrm{adv}} = \rho C_{\mathrm{P}}\boldsymbol{v}\delta T = -k_{\mathrm{v}}\left(\boldsymbol{\nabla}T - \boldsymbol{\nabla}T_{\mathrm{S}}\right), \tag{4}$$

where δT is the local temperature perturbation and k_{v} is an effective conductivity due to thermal convection.

The heat conservation/temperature equation (Eq. [2]) is a well-studied partial differential equation (PDE). In this work, we use Eq. [2] to calculate the thermal structure of convective systems within the framework of mixing-length theory. In order to solve such equations numerically, boundary conditions have to be specified. With respect to the type of the numerical problem presented in this study, we enforce constant temperature conditions at the upper and lower thermal boundaries. The question of finding a solution for Eq. [2] is known as the Dirichlet problem.

As mentioned in the introduction, the basic idea of the mixing-length theory (Taylor 1915; Prandtl 1925) is that a thermal parcel migrates for a characteristic length scale before dispersing into the surrounding fluid. Thus, the mixing length is conceptually analogous to the mean free path in thermodynamics. Therefore, the effective thermal diffusivity κ_{v} can be defined as

$$\kappa_{\mathrm{v}} = vl, \tag{5}$$

where v is the velocity of the thermal parcel and l is the mixing length, which is assumed to be identical to the size of the thermal parcel (Yamagishi & Yanagisawa 2001-2002). The effective thermal conductivity k_{v} is then given as

$$k_{\mathrm{v}} = \rho C_{\mathrm{P}}\kappa_{\mathrm{v}} = \rho C_{\mathrm{P}}vl. \tag{6}$$

According to the extended mixing-length theory (Sasaki & Nakazawa 1986), the vertical motion of a thermal parcel is constrained by the Stokes' flow. Therefore, the velocity v of such a parcel can be written as

$$v = \frac{\alpha\rho gl^{2}}{18\eta}\delta T, \tag{7}$$

where α is the thermal expansivity, g is the acceleration due to gravity, η is the dynamic viscosity, δT is the difference between the temperature of the thermal parcel and the temperature of the surrounding fluid. The temperature perturbation δT can be estimated as

$$\delta T = (\nabla T_{\mathrm{S}} - \nabla T)\, l, \tag{8}$$

where ∇T_{S} represents the adiabatic temperature gradient and ∇T denotes the local temperature gradient.

Inserting Eq. [8] into Eq. [7] yields for the velocity v the following expression:

$$v = \frac{\alpha \rho g l^3}{18\eta} (\nabla T_{\mathrm{S}} - \nabla T). \tag{9}$$

With Eq. [9], the effective thermal conductivity k_{v} can then be expressed as

$$k_{\mathrm{v}} = \rho C_{\mathrm{P}} v l = \frac{\alpha \rho^2 C_{\mathrm{P}} g l^4}{18\eta} (\nabla T_{\mathrm{S}} - \nabla T). \tag{10}$$

Since both thermal gradients are defined negative, but k_{v} must be zero or larger, Eq. [10] equals zero for $|\nabla T_{\mathrm{S}}| \geq |\nabla T|$. Otherwise, for $|\nabla T_{\mathrm{S}}| < |\nabla T|$, the advective heat flux is then calculated with Eq. [4].

In the original formulation of the mixing-length theory according to Sasaki & Nakazawa (1986), the characteristic mixing length is given by the pressure scale height. Based on experimental evidence, Abe (1995) subsequently introduced the distance to the nearest thermal boundary as a simple but sufficient approximation to assess the magnitude of the mixing length. In order to calibrate the mixing length l, we instead adopt a similar form to what was suggested by Kamata (2018):

$$l = \begin{cases} \alpha_{\mathrm{MLT}} \left(\dfrac{h}{\beta_{\mathrm{MLT}}} \right) & \text{for } h \leq \dfrac{D}{2} \beta_{\mathrm{MLT}} \\[2ex] \alpha_{\mathrm{MLT}} \left(\dfrac{D-h}{2-\beta_{\mathrm{MLT}}} \right) & \text{for } h > \dfrac{D}{2} \beta_{\mathrm{MLT}}, \end{cases} \tag{11}$$

where h is the height above the core-mantle boundary, D is the thickness of the entire mantle (including non-convecting parts), and α_{MLT} and β_{MLT} are tunable parameters.

Figure 1 illustrates how the two parameters α_{MLT} and β_{MLT} modify the mixing length. The first calibration parameter controls the magnitude of the local mixing length. A higher value of α_{MLT} leads to steeper gradients in the mixing-length distribution, which will affect in particular the thermal convection close to the domain boundaries. The second calibration parameter determines

the peak depth of the mixing-length distribution. A higher value of β_{MLT} shifts the peak depth from left to right, i.e., towards the planetary surface. We demand that α_{MLT} is either zero or greater than zero and β_{MLT} takes a value between zero and two. The conventional mixing-length formulation according to Abe (1995) is reproduced, if both calibration parameters equal unity.

2.2 Three-dimensional Simulations of Mantle Convection

For the calibration itself, we rely on the finite-volume code Gaia (Hüttig & Stemmer 2008; Hüttig et al. 2013), which has been used to carry out convection experiments in a three-dimensional (3-D) spherical geometry. Gaia solves the conservation equations with respect to the extended Boussinesq approximation (EBA). EBA distinguishes itself from the well-known Boussinesq approximation simply in that adiabatic heating and viscous dissipation are taken into account in the energy conservation equation. The density ρ is assumed to be constant so that the fluid is still incompressible. The non-dimensional conservation equations of mass, linear momentum and thermal energy read (Christensen & Yuen 1985; Ismail-Zadeh & Tackley 2010):

$$\boldsymbol{\nabla} \cdot \boldsymbol{v} = 0, \tag{12}$$

$$\boldsymbol{\nabla} \cdot \left[\eta \boldsymbol{\nabla} \boldsymbol{v} + \eta (\boldsymbol{\nabla} \boldsymbol{v})^T \right] - \boldsymbol{\nabla} p + \mathrm{Ra} T \boldsymbol{e}_{\mathrm{r}} = 0, \tag{13}$$

$$\frac{DT}{Dt} - \boldsymbol{\nabla} \cdot (\boldsymbol{\nabla} T) - \mathrm{Di}(T + T_0) v_{\mathrm{r}} - \frac{\mathrm{Di}}{\mathrm{Ra}} \Phi - H = 0, \tag{14}$$

where $\boldsymbol{v}$ is the velocity vector and v_{r} its radial component, p the dynamic pressure, T the temperature, T_0 the surface temperature, t the time, η the viscosity, $\boldsymbol{e}_{\mathrm{r}}$ the radial unit vector, and $\Phi \equiv \boldsymbol{\tau} : \dot{\boldsymbol{\varepsilon}}/2$ the viscous dissipation, with $\boldsymbol{\tau}$ and $\dot{\boldsymbol{\varepsilon}}$ denoting the deviatoric stress and strain-rate tensors, respectively. Ra is the thermal Rayleigh number, H the internal heating rate, which is given by the ratio of Ra_{Q} and Ra, where Ra_{Q} is the Rayleigh number for internal heat sources. The boundary conditions are free-slip along all boundaries.

Depending on the heating mode, we use the following formulations of the Rayleigh and Nusselt number. In case of bottom heating, internal heating rate equals zero and the Rayleigh number Ra is given by:

$$\mathrm{Ra} = \frac{\alpha \rho g \Delta T D^3}{\kappa_{\mathrm{c}} \eta_{\mathrm{b}}}, \tag{15}$$

where ΔT is the temperature difference between the temperature at the bottom T_{b} and top T_{t} of the mantle. For mixed-mode heating, i.e. heating from below and from within, the Rayleigh number $\mathrm{Ra_Q}$ associated with internal heat sources is defined as:

$$\mathrm{Ra_Q} \quad = \quad \frac{\alpha \rho^2 g H D^5}{\kappa_{\mathrm{c}} k_{\mathrm{c}} \eta_{\mathrm{b}}}. \tag{16}$$

The conductive temperature profile used to compute the Nusselt numbers is given by (Schubert et al. 2001):

$$T(r) \quad = \quad -\frac{\rho H r^2}{6 k_{\mathrm{c}}} + \frac{c_1}{r} + c_2 \tag{17}$$

where c_1 and c_2 are constants determined by boundary conditions. The Nusselt number for the top and bottom boundary is then calculated by dividing the total heat flux across the boundaries by the conductive heat flux at the top and bottom boundary, respectively:

$$\mathrm{Nu} \quad = \quad \frac{\bar{q}}{q_{\mathrm{c}}} \tag{18}$$

And hence, the Nusselt number at the outer boundary of the spherical shell reads

$$\mathrm{Nu_t} \quad = \quad -\frac{q_{\mathrm{t}} r_{\mathrm{t}} D}{r_{\mathrm{b}} k_{\mathrm{c}} \Delta T} \tag{19}$$

for bottom heating and

$$\mathrm{Nu_t} \quad = \quad -\frac{6 q_{\mathrm{t}} r_{\mathrm{t}} D}{2 r_{\mathrm{t}}^2 \rho H D - r_{\mathrm{b}}^2 \rho H D - r_{\mathrm{b}} r_{\mathrm{t}} \rho H D + 6 r_{\mathrm{b}} k_{\mathrm{c}} \Delta T} \tag{20}$$

for mixed-mode heating.

For the dynamic viscosity η, we adopt the following law with a strong temperature dependence (Miyagoshi et al. 2015):

$$\eta(T) \quad = \quad \eta_{\mathrm{t}} \left(\frac{\eta_{\mathrm{b}}}{\eta_{\mathrm{t}}} \right)^{\frac{T_{\mathrm{t}} - T}{T_{\mathrm{t}} - T_{\mathrm{b}}}}, \tag{21}$$

where η_{t} and η_{b} denote the viscosity at top and bottom of the model, respectively. During all model simulations, the thermal expansivity α, the thermal conductivity k_{c}, the thermal diffusivity κ_{c}, the gravitational acceleration g, and the density ρ have been held constant. The modeling parameters are summarized in Tab. 1.

3 RESULTS AND DISCUSSION

3.1 Conventional Mixing-length Theory

The conventional formulation of mixing-length theory defines the local mixing length as the distance to the nearest thermal boundary layer (Abe 1995). Figure 2 shows a comparison of the conventional MLT with results of fully dynamic convection simulations. The numerical simulation experiments compiled in Tab. 2 are subdivided into three characteristic modes of convection determined by using the Péclet number. Different heating modes and convective regimes are shown by different symbols.

The Péclet number (Pe) is a dimensionless number that gives the ratio of the advective to the diffusive transport rate and can be written as follows:

$$\text{Pe} \quad = \quad \frac{\lambda v_{\mathrm{ms}}}{\kappa_{\mathrm{c}}}, \tag{22}$$

where λ is the characteristic length scale, κ_{c} is the thermal diffusivity, and v_{ms} is the maximum velocity of the surface. If Pe is small, heat transfer by thermal conduction is important. The characteristic modes of convection are then classified as follows (see, Noack & Breuer (2013)): (a) whole-layer convection ($\text{Pe} \geq 100$), (b) transitional convection ($1 < \text{Pe} < 100$), and (c) convection beneath a conductive lid ($\text{Pe} \leq 1$). The surface corresponding to the former two regimes is mobile, whereas that of the latter is immobile. Therefore, we refer to as mobile-lid convection for all cases with Péclet numbers about or greater than 100 and to as stagnant-lid convection when Pe is about or smaller than 1. The remaining cases with Péclet numbers between 1 and 100 correspond to a sluggish-lid regime.

Comparing Nusselt numbers obtained from employing the convectional MLT to those provided by the numerical simulation experiments (Fig. 2(a)), we find that the conventional formulation of mixing length does not yield satisfactory results. The mismatch between predictions of MLT and reference values from fully dynamic simulations is as large as 60%, which would be of the order of 60 mW/m^2 for the heat flux through the oceanic crust on Earth. For bottom heating, MLT underestimates the heat flux in the mobile-lid regime and always overestimates the heat flux in the stagnant-lid regime for both heating modes. Therefore, calculated Nusselt numbers according

to the conventional mixing-length theory may be inaccurate. Without appropriate calibration this approach provides at best a crude approximation for the surface heat flux and thermal evolution of planetary bodies.

A similar picture is obtained when looking at the average temperature of the convective system, although the discrepancy between conventional MLT and numerical simulation experiments is considerably smaller. Figure 2(b) illustrates this by showing average temperatures according to the conventional MLT in comparison to those provided by the numerical simulation experiments. The mismatch between predictions of MLT and reference values from fully dynamic simulations is as large as 20%, which corresponds to a difference of $\sim$700 K in the average mantle temperature of an Earth-like planet. For mixed-mode heating, MLT systematically underestimates average temperature in sluggish-lid and stagnant-lid regimes. Other than that, MLT yields temperatures scattering around our reference values.

Although MLT with its conventional formulation for the mixing length does provide only a rough estimate for surface heat flux and average temperature of a convecting mantle, Fig. 3 illustrates that the method is capable of producing plausible distributions of temperature. The influence of the Rayleigh number on the temperature profile is shown in Fig. 3(a). High Rayleigh numbers yield steep temperature gradients in the upper and lower thermal boundary layer, where heat is transferred solely by conduction. Furthermore, an adiabatic temperature rise is present in the mid-region of convective system. Low Rayleigh numbers produce more gradually increasing temperature profiles that are characteristic of thermal conduction throughout the whole system. As predicted by theoretical considerations, the thickness of thermal boundaries decreases for higher Rayleigh numbers, which correspond to higher Nusselt numbers. Vice versa, increasingly thicker thermal boundaries are correlated with lower Rayleigh and Nusselt numbers.

Since the ratio of core to surface area is smaller in a spherical shell geometry compared to a Cartesian box domain, the interior temperature of the former is characteristically smaller. Therefore, we observe a substantially larger temperature increase within the thermal boundary layer at the bottom, compared to that of the top thermal boundary layer. For isoviscous models with rectangular geometry, the temperature profile would be symmetric with respect to the center of the

convective system. Figure 3(b) illustrates how the distribution of temperature changes due to a higher viscosity contrast. A higher viscosity contrast results in higher temperatures in the interior, thicker thermal boundary layers, and a steeper adiabatic temperature increase in the mid-region. The latter can be explained by an increased tendency towards sluggish-lid convection within the system because of larger effective viscosity.

3.2   Calibration Parameters

In order to precisely compute the thermal structure of rocky planets within the framework of mixing-length theory, we introduce the tunable parameters α_{MLT} and β_{MLT} to calibrate the local mixing length through comparison with fully dynamic convection simulations. These two calibration parameters affect the calculation of key parameters such as Nusselt number and average temperature, which eventually determine the thermal evolution of planets. Figure 4 shows the effects of α_{MLT} and β_{MLT} for two scenarios using a Rayleigh number $\mathrm{Ra_b}$ of 10^7 and a viscosity contrast $\Delta\eta_{\mathrm{T}}$ of 10^3, and assuming a bottom-heated (panel a) and a mixed-heated (panel b) system, respectively. For reference, the black star in each panel indicates the Nusselt number and average temperature calculated based to the conventional formulation of mixing-length theory, where the local mixing length is equivalent to the distance to the nearest thermal boundary layer.

As it can be seen in Fig. 4, α_{MLT} has a strong impact on the Nusselt number, whereas β_{MLT} influences mainly the average temperature of the convective system. Independent of the heating mode, higher values of α_{MLT} yield higher Nusselt numbers. The effect of α_{MLT} on average temperature is less pronounced. For bottom heating (Fig. 4(a)), higher values of α_{MLT} increase the average temperature, while for mixed-mode heating (Fig. 4(b)), higher values of α_{MLT} lead to a lower average temperature of the convective system. Small values of β_{MLT} lead to high average temperatures, independent of the heating mode. However, the increase in average temperature with decreasing β_{MLT} is much less pronounced in cases employing mixed-mode heating (Fig. 4(b)) because they possess in general high average temperatures when compared to bottom-heated systems. Nusselt number is also influenced by β_{MLT}, but for a lesser extent.

3.3   Calibrated Mixing-length Theory

We calibrate the mixing length through comparison with the statistical equilibrium states of convection simulations in such a way that Nusselt numbers and average temperatures of Tab. 2 are reproduced by mixing-length theory as accurately as possible. The calibration parameters α_{MLT} and β_{MLT} are simultaneously determined by a least-squares minimization technique employing the simplex search method of Lagarias et al. (1998). Results of the calibration are presented in Tab. 3 for bottom and mixed-mode heating, respectively. The two tables list the optimal values of the calibration parameters α_{MLT} and β_{MLT}.

How good the calibrated mixing-length theory performs against our fully dynamic convection simulations is shown in Fig. 5. With the derived calibration, MLT reproduces both Nusselt number and average temperature with discrepancies well below 1% for all bottom-heated cases. All non-filled symbols align perfectly with the straight black lines in both panels of Fig. 5. For mixed-mode heating, Nusselt numbers are reproduced with similar accuracy (Fig. 5(a)). However, a few cases corresponding to sluggish-lid convection still show discrepancies as large as 10% for the average temperature of the convective system (Fig. 5(b)). This shows that the piecewise linear approximation of the mixing length cannot capture all dynamical effects forming in the sluggish-lid regime in the simulations with mixed-mode heating. Nonetheless, using the presented calibration within the framework of MLT provides a significant improvement over the conventional formulation of mixing length.

3.3.1   *Maps of α_{MLT} and β_{MLT}*

A three-dimensional surface has been fitted to each dataset of calibration values using a bicubic interpolation. The threshold for the onset of thermal convection in spherical shells heated from below is yet adopted from Kameyama et al. (2013). Furthermore, our numerical simulations reveal that this threshold represents also an acceptable approximation for spherical shells with mixed-mode heating. The resulting calibration maps of α_{MLT} and β_{MLT} shown in Fig. 6 make the mixing-length theory applicable to any combination of Rayleigh number and viscosity contrast. In general, we find that mixing length is sensitive to both viscosity contrast and Rayleigh number. The efficiency

of heat transport is correlated to convective modes representing different types of thermal convection. These discrete regimes are reflected within the pattern of calibration values and clearly visible in Fig. 6. We can distinguish between them and identify where transitions from one regime into another occur, because the slope of the surface fits substantially change at the boundaries between convective modes, especially between the stagnant-lid to mobile-lid regime.

Panels (a) and (c) in Fig. 6 show the derived values for calibration parameter α_{MLT} that governs the absolute magnitude of mixing length. By inspecting both panels we find that the pattern of how these values are distributed shows the same features for both heating modes. For any given Rayleigh number, α_{MLT} always decreases with increasing viscosity contrast. This observation represents the well-known fact that for a higher viscosity contrast the convective velocity decrease, the thermal boundary layer thickens, the thermal gradient within that boundary flattens, and as a consequence the heat transport by convection becomes less efficient. For a given viscosity contrast up to 10^4, α_{MLT} first increases rapidly from the boundary of no convection until a certain peak value was reached and afterwards α_{MLT} gradually decreases towards higher Rayleigh numbers. Peak values of α_{MLT} fall largely within the transitional regime corresponding to sluggish-lid convection. For a given viscosity contrast above 10^4, α_{MLT} gradually increases toward higher Rayleigh numbers. Care must be taken with extrapolation beyond the range where data are provided.

Panels (b) and (d) in Fig. 6 show the derived values for calibration parameter β_{MLT} that determines the peak depth of mixing length. The pattern of how these values are distributed is substantially different for the two heating modes. For bottom-heated cases (Fig. 6(b)), besides the apparent valley at medium Rayleigh numbers and high viscosity contrasts, the landscape of the pattern is for the most part flat. Slightly elevated values of β_{MLT} are primarily observed in the transitional regime close to the boundary of convection breakdown and at medium Rayleigh numbers and viscosity contrasts. However, most values cluster around 1, which implies that peak depth of the mixing length is found in the mid-region of a convective system. Cases located in the valley possess low values of β_{MLT} and are clearly correlated to the stagnant-lid regime, in which the transport of heat through a convective system becomes much less effective in comparison to the other regimes.

For cases employing mixed-mode heating (Fig. 6(d)), the values of β_{MLT} show a canyon-like pattern. Cases located in the center of the canyon possess low values of β_{MLT} and correspond with sluggish-lid convection of the transitional regime. This is opposite to bottom-heated cases (Fig. 6(b)), for which the transitional regime has the highest values of β_{MLT}. Higher temperatures in the mid-region of the convective system are the result of internal heat sources. The cases characterized by mobile-lid convection are found at the right flank of the canyon at a Rayleigh number of at least 10^5. In the direction of higher Rayleigh numbers, peak depth of the mixing length moves rapidly towards the center of the convective system, where β_{MLT} equals 1. Cases characterized by stagnant-lid convection cluster on the left flank of the canyon at medium Rayleigh number and high viscosity contrast. They show slightly higher values for β_{MLT} when compared to the corresponding bottom-heated cases.

For bottom heating, calibration values associated with transitional regime are closer to the values obtained for whole-layer convection than to the results for the stagnant-lid regime. This suggests that the transition from the sluggish-lid regime into the stagnant-lid regime is more pronounced than the transition from sluggish to fully mobile. The finding is consistent with the fact that systems with an immobile conductive lid on top of the convecting region cool significantly slower when compare to those that allow for some kind of surface mobilization, e.g., Schubert et al. (2001).

3.3.2   *Scaling laws for α_{MLT} and β_{MLT}*

Table 4 provides scaling laws for the calibrated α_{MLT} and β_{MLT} as a function of Rayleigh number and viscosity contrast. In addition, the resulting maps of the two calibration parameters are shown in Fig. 7. The analytical expressions provided in Tab. 4 are fully empirical as we are not attempting here to derive a physical model of α_{MLT} and β_{MLT}. Nusselt number and average temperature of the convective system are reproduced by the simple parameterization for α_{MLT} and β_{MLT} with discrepancies within 10% when compared to the numerical simulation experiments. Our scaling laws offer a significant improvement in accuracy, as opposed to 60% and 20% respectively using the conventional mixing length.

Our analytical formulations of α_{MLT} and β_{MLT} can yet be used outside the range of our numerical simulations as we chose smooth functions which do not diverge away from the fitted parameter range. Because of fundamental differences between the convection regimes, it is challenging to consolidate all three regimes into a simple scaling parameterization. Therefore, we subdivide each dataset of α_{MLT} and β_{MLT} into two corresponding to (a) whole-layer/transitional convection and (b) convection beneath an immobile conductive lid. The discontinuity between these two regimes has been established in accordance with the Péclet numbers of the numerical simulations (Tab. 2) and is illustrated with the thick black boundary line in Fig. 7.

Our empirical expressions for α_{MLT} given in Tab. 4 are identical in shape for both heating modes. The parameter α_{MLT} can be described as a steep cliff close to the critical Rayleigh number which transitions into a slightly sloping plateau at larger Rayleigh numbers. For mobile and sluggish cases, we find that β_{MLT} can be reasonably fitted by using a hyperbolic tangent in the Rayleigh number space. We observe that the parameter β_{MLT} slightly decreases with the Rayleigh number for the bottom-heated simulations, whereas it increases with the Rayleigh number for the mixed-mode heating. In the stagnant-lid regime, we fit β_{MLT} with a plane in logarithmic spaces of both Rayleigh number and viscosity contrast. More numerical investigations would be required to confirm the trends provided by Kamata (2018) who reported an exponential decrease of α_{MLT} and β_{MLT} with increasing viscosity contrast in the stagnant-lid regime.

Although mixing-length theory would provide a reasonably-looking solution using an extrapolated mixing length, we cannot estimate the misfit between such solution and the output of a numerical simulation using the according Rayleigh number and viscosity contrast. However, we can compare our extrapolations with existing Nusselt-Rayleigh scaling laws; at least for the extensively studied case of isoviscous fluids. In doing so, we fit isoviscous simulations of the calibrated MLT with Rayleigh number $\mathrm{Ra_b}$ up to 10^{10} to the following relationship:

$$\mathrm{Nu} \;=\; a \left(\frac{\mathrm{Ra}}{\mathrm{Ra}_c} \right)^b, \tag{23}$$

where a and b represent fitting coefficients and Ra_c is the critical Rayleigh number. A critical Rayleigh number of about 10^3 is derived from linear stability analysis, e.g., Schubert et al. (2001). However, the results are relatively insensitive to the choice of Ra_c (Weller et al. 2016).

For bottom heating, we find for a and b the values 1.4 and 0.29, respectively. The exponent b of the Nusselt-Rayleigh scaling law is in good agreement with the range of 0.26 to 0.29 suggested by similar numerical simulations (Wolstencroft et al. 2009; Deschamps et al. 2010). However, b is lower when compared to the analytically found relationship of $\mathrm{Nu} \propto \mathrm{Ra}^{1/3}$ for fluids heated from below (Solomatov 1995).

For mixed-mode heating, we obtain for a and b in Eq. [23] the values 0.85 and 0.19, respectively. This exponent b for thermal convection in spherical geometry is significantly lower when compared to the one reported by Deschamps et al. (2010). However, the heating rate that we are using is lower than the lowest value of Deschamps et al. (2010) (3.6975 vs. 5.0 - 40), so our cases are closer to the bottom-heated cases of Deschamps et al. (2010) and Deschamps & Sotin (2001). In the latter study, the authors report an exponent as small as 0.21. An additional difference between the cases presented here and the ones of Deschamps et al. (2010) is that we are using adiabatic heating and cooling (EBA).

3.3.3   *Comparison of numerical and calibrated temperature profiles*

A detailed comparison between distributions of temperature according to mixing-length theory and numerical simulation experiments is given in Fig. 8. The mixing-length formalism is capable of generating temperature profiles in reasonable agreement with 3-D numerical simulations, if a proper calibration for the mixing length is used (blue solid curves).

For mobile-lid convection (Fig. 8(a) and (d)), the largest discrepancy between calibrated MLT and numerical experiments is found at the top of the bottom boundary layer. In this region, we observe a difference in temperature as large as a few hundred Kelvin. The offset can be explained by considering lateral motion of the fluid in a three-dimensional geometry, which strongly affects the temperature distribution close to thermal boundary layers and can even cause locally a negative temperature gradient (e.g., Fig. 8(d)). Such effects cannot be reproduced by the one-dimensional MLT, however our calibration still allows to fit the Nusselt numbers and internal temperature, which control the thermal evolution of planets. For thermal convection corresponding to the transitional regime (Fig. 8(b) and (e)), temperature distributions show discrepancies either at the top

of the lower thermal boundary layer (for bottom heating, Fig. 8(b)), or in the mid-region of the convective system, if none or only a shallow bottom thermal boundary exists (for mixed-mode heating, Fig. 8(e)). Finally, for stagnant-lid convection (Fig. 8(c) and (f)), discrepancies between calibrated MLT and numerical experiments are almost non-existent.

Upon comparison with numerical experiments, our calibrated MLT models (blue solid curves) show a considerable improvement against the models relying on the conventional mixing-length formulation (red dashed curves), in particular for whole-layer convection characterized by a small viscosity contrast (Fig. 8(a) and (d)) and convection beneath an immobile conductive lid emerging at a large viscosity contrast (Fig. 8(c) and (f)). Thermal gradients within the boundary layers are more accurately reproduced by a calibrated mixing length and lead to a better agreement of the general temperature distributions (e.g., Fig. 8(a) and (c)). Furthermore, average temperatures characterizing the thermal structure in the mid-region of the convective system are also in better agreement with results from convection simulations (e.g., Fig. 8(b) and (e)).

3.3.4 Depth-dependent viscosity

Five additional simulations employing a depth-dependent viscosity were performed as a test. Our approach was able to obtain very good regressions of the Nusselt number and the temperature profile without need for additional complexity (and with accuracy identical to the previous cases). The four first cases employ a gradual increase of viscosity with depth:

$$\eta(T, d) \;=\; \eta_{\mathrm{t}} \left(\frac{\eta_{\mathrm{b}}}{\eta_{\mathrm{t}}} \right)^{\frac{T_{\mathrm{t}} - T}{T_{\mathrm{t}} - T_{\mathrm{b}}}} \Delta\eta_{\mathrm{d}}^{\frac{d}{D}}, \tag{24}$$

where d is depth and $\Delta\eta_d$ is the viscosity contrast. The last case employs a viscosity jump at mid-mantle depth. No internal heating was used in these tests. Table 5 shows the calibration coefficients α and β obtained together with the Nusselt number and average temperature from the direct 3-D numerical simulations. To compare the simulations with depth-dependent viscosity with the purely temperature-dependent ones, we use the bottom Rayleigh number and the viscosity contrast between top and bottom of the domain (which is equivalent to what is shown in Fig. 6).

We observe that all simulations employing a viscosity contrast inferior to 10^4 are well reproduced by a coefficient α close to 1.9. Figure 6 showed that α decreases for increasing thermal

viscosity contrast. Interestingly, this result does not seem to apply to the depth dependence of the viscosity. This indicates that α depends more on $\Delta\eta_T$ than $\Delta\eta_d$. Furthermore, we observe that α decreases to 0.949 when the top to bottom viscosity contrast is 10^4. This corresponds to the case 19 in Fig. 6 which has the identical viscosity contrast and bottom Rayleigh number and was found to be best fitted with a coefficient α of 1.09.

For a viscosity which does not depend solely on temperature, we find that for a viscosity contrast inferior to 10^4 the calibration coefficient β slightly increases with increasing depth dependence of the viscosity. Table 5 also shows that β weakly depends on the thermal viscosity contrast, which is consistent with the results depicted in Fig. 6 for top to bottom viscosity contrast inferior or equal to 10^4.

3.3.5   *Time dependence of the solution*

The mixing-length formalism provides the evolution of temperature at each point of the profile (Eq. [2]). Computing the time dependence of the solution is therefore straightforward. Figure 9 depicts a comparison between the average temperature obtained with the direct 3-D numerical simulations and with the mixing-length approach. We see that our calibrated mixing length is able to reproduce the appropriate kinetics of evolution of the temperature profile according to two selected examples.

The blue curves in Fig. 9 show that mixing-length theory can capture the natural time scale of the system as the temperature decrease is similar. However, MLT cannot reproduce strong time non-linearities like overshoots or periodic behaviors. This limitation also unfortunately applies to boundary-layer theory. Since a linear temperature profile was used as initial condition in our 3-D simulations, Fig. 9 shows that mixing-length theory gets to a very accurate equilibrium using a different process than overturns naturally occurring in the 3-D simulations. Instead, the mixing-length model builds boundary layers to equilibrium using only 1-D processes: gradual growth of boundary layers and homogenization of the internal temperature. Very non-dynamically consistent initial temperature fields are therefore difficult to reproduce accurately using MLT, but the evolution kinetics is still satisfyingly captured.

4 CONCLUSION AND CRITICAL COMMENTS

Reliable estimates of heat flux and temperature for the viscous mantle are essential when computing the thermal state of planetary bodies. In particular if geophysical processes on terrestrial planets such as the generation of self-sustained magnetic fields are of interest, mixing-length theory could be a solid method to gather important information from large ensembles of planet models covering a wide parameter space. Therefore, we focused in this study on the extension of MLT for highly viscous fluids (Sasaki & Nakazawa 1986; Abe 1995) to calculate the heat flux of convective systems and to obtain a corresponding radial temperature distribution.

Building on the work of Kamata (2018), we thoroughly calibrate the mixing-length parameter of the local mixing-length theory by comparison to fully dynamic simulations, which have been carried out with the mantle convection code Gaia. We thereby lay our focus on a 3-D spherical geometry with an inner to outer core radius that mimics the ratio of the Earth. The ultimate goal of this exercise is to derive simple but accurate parameterizations for the mixing length, describing the heat transport of different convective regimes of planetary mantles. The calibration derived in this study is only fully valid for Earth-like planets heated either from below or from below and within. Differences in geometry and/or heating mode should result in different parameterizations for the local mixing-length. We also expect that the time-varying distribution of heat producing elements in a convecting system may further complicate possible parameterizations of thermal convection. Furthermore, we have limited ourselves to a temperature-dependent viscosity only. However, viscosity depends not only on temperature but also on pressure, although the pressure effect is heavily debated in current literature, e.g., Karato (2011). More numerical investigation is therefore needed to provide generalized scaling laws for α_{MLT} and β_{MLT} parameters.

In the mobile-lid regime, the present study showed that a carefully calibrated MLT is now capable of reproducing the thermal structure suggested by our numerical simulation experiments with good accuracy, thereby significantly improving a single-parameter calibration of Tachinami et al. (2011) obtained from Nusselt-Rayleigh scaling laws. For the special case of an isoviscous fluid ($\Delta\eta_{\mathrm{T}} = 10^0$), mixing length has to be significantly larger when compared to its conventional formulation of Abe (1995). With respect to this calibration, mixing-length theory produces results

in good agreement to those predicted by phenomenological Nusselt-Rayleigh scaling laws for thermal convection.

In the stagnant-lid regime, we demonstrated that the conventional mixing-length formulation cannot simultaneously reproduce heat flux and average temperature of our numerical simulations with sufficient accuracy. This finding challenges the study of Kimura et al. (2009), in which it is claimed that the transition from mobile-lid to stagnant-lid convection naturally arises from mixing-length theory (cf. figure 9 of their original work). Nonetheless, the present study provides an appropriate calibration for the local mixing-length parameter that makes mixing-length theory also perfectly applicable to stagnant-lid convection. For stagnant-lid convection, mixing length is substantially lower and its peak depth is found at greater depths, when compared to the original formulation of Abe (1995). These results are in good agreement with the findings of Kamata (2018).

In the sluggish-lid regime, we find that a calibrated mixing-length theory cannot always accurately reproduce the temperature profile of our numerical simulations even though our calibration increases the quality in comparison to the conventional formulation by at least a factor of 2. This is however expected as large temperature and viscosity lateral variations develop in this regime (only). It cannot be expected that such 3-D effects can be perfectly accounted for in the framework of a 1-D model.

Adding internal heat sources into a convective model introduces additional asymmetry in both the stream function and temperature fields (Jarvis & Peltier 1989). According to our numerical convection simulations, Nusselt numbers decrease on average, whereas average temperatures increase on average, when uniformly distributed heat sources are added into the convective system. Consequently, the presence of internal heat sources strongly affects the calibration, in particular the calibration parameter controlling the peak depth of the mixing length.

In summary, the mixing-length theory is a simple and fast approach to calculate surface heat fluxes and radial temperature distributions for rocky planets considered at quasi-static equilibrium. Such methods are essential when huge ensembles of newly discovered exoplanets have to be processed to constrain their internal structure and chemical composition using Bayesian analysis,

e.g., Dorn et al. (2015). With the new calibration, a mixing-length parameterization of convective heat transport is established as an alternative approach to the widely used boundary-layer theory. The present parameterization covers a large range of Rayleigh numbers and viscosity contrasts widely used in the literature to model the interior dynamics of terrestrial planets (Schubert et al. 2001; Tosi et al. 2014). Since the method relies on local values of physical quantities, the mixing-length theory yields a better spatial resolution when compared to other parameterized convection models (Tachinami et al. 2011). Internal heating, e.g., due to the decay of radiogenic elements or the dissipation of tidal energy, can be taken into account easily by adding a heat generation term to the advection-diffusion equation. Thus, the mixing-length theory is well suited for calculating the thermal structure of terrestrial planets including rocky exoplanets, which may exhibit radial compositional changes and pressure-induced phase transitions acting as convective boundaries.

REFERENCES

Abe, Y., 1995. *The Earth's Central Part: Its Structure and Dynamics*, chap. Basic equations for the evolution of partially molten mantle and core, pp. 215–230, TERRAPUB.

Abe, Y., 1997. Thermal and chemical evolution of the terrestrial magma ocean, *Phys. Earth Planet. Inter.*, **100**, 27–39.

Christensen, U. R. & Yuen, D. A., 1985. Layered convection induced by phase transitions, *J. Geophys. Res.*, **90**, 10,291–10,300.

Deschamps, F. & Sotin, C., 2001. Thermal convection in the outer shell of large icy satellites, *J. Geophys. Res.: Planets*, **106**, 5107–5121.

Deschamps, F., Tackley, P. J., & Nakagawa, T., 2010. Temperature and heat flux scalings for isoviscous thermal convection in spherical geometry, *Geophys. J. Int.*, **182**, 137–154.

Dorn, C., Khan, A., Heng, K., Connolly, J. A. D., Alibert, Y., Benz, W., & Tackley, P., 2015. Can we constrain the interior structure of rocky exoplanets from mass and radius measurements?, *Astron. & Astrophys.*, **577**, A83.

Gerya, T., 2010. *Introduction to Numerical Geodynamic Modelling*, Cambridge University Press.

Hansen, C. J., Kawaler, S. D., & Trimble, V., 2004. *Stellar Interiors: Physical Principles, Structure, and Evolution*, Springer.

Holton, J. R. & Hakim, G. J., 2013. *An Introduction to Dynamic Meteorology*, Elsevier Academic Press.

Hüttig, C. & Stemmer, K., 2008. Finite volume discretization for dynamic viscosities on Voronoi grids, *Phys. Earth Planet. Inter.*, **171**, 137–146.

Hüttig, C., Tosi, N., & Moore, W. B., 2013. An improved formulation of the incompressible Navier-Stokes equations with variable viscosity, *Phys. Earth Planet. Inter.*, **220**, 11–18.

Ismail-Zadeh, A. & Tackley, P., 2010. *Computational Methods for Geodynamics*, Cambridge University Press.

Jarvis, G. T. & Peltier, W. R., 1989. *Mantle Convection: Plate Tectonics and Global Dynamics*, chap. Convection models and geophysical observations, pp. 479–594, Gordon and Breach Science Publishers.

Kamata, S., 2018. One-dimensional convective thermal evolution calculation using a modified mixing length theory: Application to Saturnian icy satellites, *J. Geophys. Res.: Planets*, **123**, 93–112.

Kameyama, M., Ichikawa, H., & Miyauchi, A., 2013. A linear stability analysis on the onset of thermal convection of a fluid with strongly temperature-dependent viscosity in a spherical shell, *Theor. Comput. Fluid Dyn.*, **27**, 21–40.

Karato, S., 2011. Rheological structure of the mantle of a super-Earth: Some insights from mineral physics, *Icarus*, **212**, 14–23.

Kimura, J., Yamagishi, Y., & Kurita, K., 2007. Tectonic history of Europa: Coupling between internal evolution and surface stresses, *Earth Planets Space*, **59**, 113–125.

Kimura, J., Nakagawa, T., & Kurita, K., 2009. Size and compositional constraints of Ganymede's metallic core for driving an active dynamo, *Icarus*, **202**, 216–224.

Lagarias, J. C, Reeds, J. A., Wright, M. H., & Wright, P. E., 1998. Convergence properties of the Nelder-

Mead simplex method in low dimensions, *SIAM J. Optimiz.*, **9**, 112–147.

Miyagoshi, T., Kameyama, M., & Ogawa, M., 2015. Thermal convection and the convective regime diagram in super-Earths, *J. Geophys. Res.: Planets*, **120**, 1267–1278.

Noack, L. & Breuer, D., 2013. First- and second-order Frank-Kamenetskii approximation applied to temperature-, pressure- and stress-dependent rheology, *Geophys. J. Int.*, **195**, 27–46.

Poirier, J.-P., 2000. *Introduction to the Physics of the Earth's Interior*, Cambridge University Press.

Prandtl, L., 1925. Bericht über Untersuchungen zur ausgebildeten Turbulenz, *Z. angew. Math. Mech.*, **5**, 136–139.

Priestley, C. H. B., 1959. *Turbulent Transfer in the Lower Atmosphere*, The University of Chicago Press.

Sasaki, S. & Nakazawa, K., 1986. Metal-silicate fractionation in the growing Earth: Energy source for the terrestrial magma ocean, *J. Geophys. Res.*, **91**, 9231–9238.

Schubert, G., Turcotte, D., & Olsen, P., 2001. *Mantle Convection in the Earth and Planets*, Cambridge University Press.

Senshu, H., Kuramoto, K., & Matsui, T., 2002. Thermal evolution of a growing Mars, *J. Geophys. Res.*, **107**, 5118.

Sharpe, H. N. & Peltier, W. R., 1979. A thermal history model for the Earth with parameterized convection, *Geophys. J. Int.*, **59**, 171–203.

Sohl, F., Solomonidou, A., Wagner, F. W., Coustenis, A., Hussmann, H., & Schulze-Makuch, D., 2014. Structural and tidal models of Titan and inferences on cryovolcanism, *J. Geophys. Res.: Planets*, **119**, 1013–1036.

Solomatov, V. S., 1995. Scaling of temperature- and stress-dependent viscosity convection, *Phys. Fluids*, **7**, 266–274.

Stevenson, D. J., Spohn, T., & Schubert, G., 1983. Magnetism and thermal evolution of the terrestrial planets, *Icarus*, **54**, 466–489.

Tachinami, C., Senshu, H., & Ida, S., 2011. Thermal evolution and lifetime of intrinsic magnetic fields of super-Earths in habitable zones, *Astrophys. J.*, **726**, 70–88.

Taylor, G. I., 1915. Eddy motion in the atmosphere, *Phil. Trans. R. Soc. London*, **215**, 1–26.

Tosi, N., Breuer, D., & Spohn, T., 2014. *Encyclopedia of the Solar System*, chap. 9: Evolution of planetary interiors, pp. 185–208, Elsevier.

Vitense, E., 1953. Die Wasserstoffkonvektionszone der Sonne, *Z. Astrophys.*, **32**, 135–164.

Wagner, F. W., Sohl, F., Hussmann, H., Grott, M., & Rauer, H., 2011. Interior structure models of solid exoplanets using material laws in the infinite pressure limit, *Icarus*, **214**, 366–376.

Wagner, F. W., Tosi, N., Sohl, F., Rauer, H., & Spohn, T., 2012. Rocky super-Earth interiors. Structure and internal dynamics of CoRoT-7b and Kepler-10b, *Astron. & Astrophys.*, **541**, A103.

Weller, M. B., Lenardic, A., & Moore, W. B., 2016. Scaling relationships and physics for mixed heating

convection in planetary interiors: Isoviscous spherical shells, *J. Geophys. Res.: Solid Earth*, **121**, 7598–7617.

Wolstencroft, M., Davies, J. H., & Davies, D. R., 2009. Nusselt-Rayleigh number scaling for spherical shell Earth mantle simulation up to Rayleigh number of 10^9, *Phys. Earth Planet. Inter.*, **176**, 132–141.

Yamagishi, Y. & Yanagisawa, T., 2001-2002. Modelling for convective heat transport based on mixing length theory, Tech. rep., Institute for Frontier Research on Earth Evolution.

This paper has been produced using the Blackwell Scientific Publications GJI LATEX2e class file.

Table 1. Modeling parameters.

Parameter	Bottom heated	Mixed heated
r_{t}, km	6370	6370
r_{b}, km	3475	3475
D, km	2895	2895
T_{t}, K	300	300
T_{b}, K	2850	2850
ΔT, K	2550	2550
H, W kg^{-1}	–	1×10^{-12}
ρ, kg m^{-3}	4500	4500
g, m s^{-2}	10	10
C_{P}, J kg^{-1} K^{-1}	1190	1190
k_{c}, W m^{-1} K^{-1}	4	4
κ_{c}, m^2 s^{-1}	9×10^{-7}	9×10^{-7}
α, K^{-1}	3×10^{-5}	3×10^{-5}

Table 2. Numerical simulation experiments.

			Bottom heated								Mixed heated				
Case	Ra_b	$\Delta\eta_T$	T_{avg} [K]	Nu	σ_{Nu} [%]	Pe	Stationarity	**Case**	Ra_b	$\Delta\eta_T$	T_{avg} [K]	Nu_t	Nu_b	Pe	Stationarity
mobile-lid regime								*mobile-lid regime*							
1	10^5	10^0	1034	4.764	1.50	235.9	time-dependent	1	10^5	10^0	1430	1.861	-11.337	211.5	time-dependent
2	10^6	10^0	1052	10.008	1.40	737.8	time-dependent	2	10^6	10^0	1310	3.008	-27.870	543.2	time-dependent
3	10^6	10^1	1149	6.304	1.59	319.3	time-dependent	3	10^6	10^1	1535	2.118	-16.072	226.0	time-dependent
4	10^6	10^2	1170	3.956	0.78	110.3	steady-state	4	10^6	10^2	1708	1.428	-5.648	145.9	time-dependent
5	10^7	10^2	1287	7.552	1.89	351.1	time-dependent	5	10^7	10^1	1342	3.306	-37.095	756.0	time-dependent
6	10^7	10^3	1361	4.583	0.88	237.1	time-dependent	6	10^7	10^2	1554	2.291	-19.711	361.4	time-dependent
7	10^8	10^3	1389	8.445	2.61	952.2	time-dependent	7	10^7	10^3	1700	1.546	-6.986	216.4	time-dependent
8	10^8	10^4	1463	5.539	2.09	410.0	time-dependent	8	10^8	10^2	1317	3.662	-43.918	1184.5	time-dependent
9	10^9	10^4	1473	10.401	2.40	1008.9	time-dependent	9	10^8	10^3	1554	2.598	-24.975	572.9	time-dependent
10	10^9	10^5	1463	6.241	0.30	418.8	time-dependent	10	10^8	10^4	1685	1.501	-7.082	184.4	time-dependent
sluggish-lid regime								11	10^9	10^3	1264	3.820	-48.978	1770.6	time-dependent
11	10^4	10^0	996	2.660	1.58	50.6	steady-state	12	10^9	10^4	1529	2.589	-24.644	1159.5	time-dependent
12	10^4	10^1	1052	1.629	0.83	12.7	steady-state	13	10^9	10^5	1671	1.678	-10.010	163.4	time-dependent
13	$10^{4.5}$	10^2	1082	1.311	1.03	6.8	steady-state	14	10^{10}	10^4	1300	3.414	-43.418	3281.0	time-dependent
14	10^5	10^1	1070	3.288	0.06	84.1	time-dependent	15	10^{10}	10^5	1491	2.407	-27.511	1066.8	time-dependent
15	10^5	10^2	1091	2.108	0.19	22.2	steady-state	16	10^{10}	10^6	1706	1.739	-11.118	181.4	time-dependent
16	10^5	$10^{2.5}$	1087	1.600	1.06	11.5	steady-state	*sluggish-lid regime*							
17	$10^{5.5}$	10^3	1115	1.948	1.07	15.7	steady-state	17	10^4	10^0	1700	1.304	-3.252	52.9	steady-state
18	10^6	10^3	1152	2.465	2.46	32.6	steady-state	18	10^4	10^1	1811	1.133	-0.720	14.4	steady-state
19	10^6	10^4	1121	1.417	1.15	9.7	steady-state	19	10^5	10^1	1715	1.318	-3.956	83.4	steady-state
20	10^7	10^4	1318	3.437	1.85	77.2	time-dependent	20	10^5	10^2	1853	1.165	-1.203	33.4	steady-state
21	10^8	10^5	1448	3.777	3.27	83.1	time-dependent	21	10^6	10^3	1825	1.218	-2.412	48.7	time-dependent
22	10^9	10^6	1493	3.831	5.71	79.0	time-dependent	22	10^7	10^4	1791	1.243	-2.119	58.0	time-dependent
stagnant-lid regime								23	10^8	10^5	1748	1.164	-1.364	34.2	time-dependent
23	$10^{6.5}$	10^5	1245	1.344	1.10	0.2	steady-state	24	10^9	10^6	1736	1.167	-1.284	9.8	time-dependent
24	$10^{6.5}$	$10^{5.5}$	1161	1.146	1.06	0.1	steady-state	*stagnant-lid regime*							
25	10^7	10^5	1353	1.690	0.77	1.1	steady-state	25	10^6	10^4	1854	1.020	0.942	0.7	time-dependent
26	10^7	10^6	1251	1.307	0.81	0.0	steady-state	26	10^7	10^5	1838	1.041	0.538	0.4	time-dependent
27	$10^{7.5}$	$10^{5.5}$	1387	1.773	1.32	1.0	time-dependent	27	10^7	10^6	1854	1.015	0.855	0.0	time-dependent
28	10^8	10^6	1412	1.862	2.31	1.2	time-dependent	28	10^8	10^6	1812	1.055	0.198	0.3	time-dependent

Table 3. Mixing-length calibration parameters.

	Bottom heated					Mixed heated			
Case	$\mathrm{Ra_b}$	$\Delta\eta_T$	α_{MLT}	β_{MLT}	**Case**	$\mathrm{Ra_b}$	$\Delta\eta_T$	α_{MLT}	β_{MLT}
mobile-lid regime					*mobile-lid regime*				
1	10^5	10^0	1.9423	1.0607	1	10^5	10^0	2.0214	0.6898
2	10^6	10^0	2.0188	1.0311	2	10^6	10^0	1.9106	0.7930
3	10^6	10^1	1.9080	1.0041	3	10^6	10^1	1.8828	0.5642
4	10^6	10^2	1.7426	1.0771	4	10^6	10^2	1.8213	0.0647
5	10^7	10^2	1.6675	0.9375	5	10^7	10^1	1.6287	0.8809
6	10^7	10^3	1.4224	0.8728	6	10^7	10^2	1.5663	0.6590
7	10^8	10^3	1.3599	0.9317	7	10^7	10^3	1.5251	0.1573
8	10^8	10^4	1.2305	0.8537	8	10^8	10^2	1.3580	1.0698
9	10^9	10^4	1.1877	0.9675	9	10^8	10^3	1.3317	0.8102
10	10^9	10^5	0.9899	1.0474	10	10^8	10^4	1.0360	0.3914
sluggish-lid regime					11	10^9	10^3	1.0389	1.2979
11	10^4	10^0	2.0331	1.1619	12	10^9	10^4	0.9456	1.0369
12	10^4	10^1	1.6457	1.1739	13	$10^{4.5}$	10^2	1.2301	1.1768
13	$10^{4.5}$	10^2	1.2301	1.1768	14	10^{10}	10^4	0.6698	1.4036
14	10^5	10^1	1.9522	1.1217	15	10^{10}	10^5	0.5988	1.2826
15	10^5	10^2	1.7323	1.1845	16	10^{10}	10^6	0.6870	0.6016
16	10^5	$10^{2.5}$	1.4822	1.2389	*sluggish-lid regime*				
17	$10^{5.5}$	10^3	1.6194	1.2450	17	10^4	10^0	2.6740	0.0206
18	10^6	10^3	1.5188	1.1894	18	10^4	10^1	2.4299	0.2537
19	10^6	10^4	1.0948	1.2751	19	10^5	10^1	2.1162	0.0303
20	10^7	10^4	1.4435	1.0349	20	10^5	10^2	2.2231	0.1156
21	10^8	10^5	1.0994	0.8927	21	10^6	10^3	2.0070	0.0214
22	10^9	10^6	0.7908	0.9135	22	10^7	10^4	1.5768	0.0428
stagnant-lid regime					23	10^8	10^5	0.9756	0.1238
23	$10^{6.5}$	10^5	0.5101	0.3585	24	10^9	10^6	0.7511	0.1108
24	$10^{6.5}$	$10^{5.5}$	0.3817	0.4202	*stagnant-lid regime*				
25	10^7	10^5	0.6027	0.3410	25	10^6	10^4	0.4310	0.6734
26	10^7	10^6	0.3627	0.2101	26	10^7	10^5	0.4607	0.6050
27	$10^{7.5}$	$10^{5.5}$	0.5321	0.2937	27	10^7	10^6	0.2895	0.6794
28	10^8	10^6	0.4839	0.3021	28	10^8	10^6	0.4109	0.5537

Table 4. Best regression of α_{MLT} and β_{MLT}.

	Fitting parameters								Scaling equations
	Bottom heated				*Mixed heated*				**Mobile (incl. sluggish) and Stagnant**
	Stagnant		*Mobile*		*Stagnant*		*Mobile*		$\alpha = [a_0 - a_1 \lg(\Delta\eta) - a_2 \lg(Ra)] \tanh\left[a_3 \lg\left(\frac{Ra}{Ra_c}\right)\right]$
	α	β	α	β	α	β	α	β	**Mobile (incl. sluggish)**
a_0	0.927	0.930	2.550	1.059	0.794	1.167	3.642	0.699	$\beta = a_0 - a_1 \tanh\left[\lg(Ra) - a_2 - a_3 \lg(\Delta\eta)^{a_4}\right]$
a_1	0.165	0.0857	0.153	0.158	0.132	-0.0686	0.0487	-0.654	**Stagnant**
a_2	-0.0684	0.0220	0.0886	5.014	-0.0515	0.129	0.281	5.478	$\beta = a_0 - a_1 \lg(\Delta\eta) - a_2 \lg(Ra)$
a_3	3.823		2.326	0.628	1.897		3.019	0.862	**Critical Rayleigh number approximation**
a_4				0.774				0.915	$\lg(Ra_c) = 4.323 + 2.922 \tanh\left[0.243 \lg(\Delta\eta) - 0.544\right]$

Table 5. Cases employing a depth-dependent viscosity. For cases 29 to 32, the viscosity increase with depth is gradual (see, Eq. [24]). For case 33, we impose a viscosity jump at mid-mantle depth.

Case	Ra_b	$\Delta\eta_T$	$\Delta\eta_d$	$\Delta\eta_{top-bot}$	T_{avg} [K]	Nu	α_{MLT}	β_{MLT}
29	10^6	1	10^1	10^{-1}	851.35	11.915	1.8937	1.1089
30	10^6	10^3	10^1	10^2	1028.9	4.0239	2.0341	1.2627
31	10^6	10^5	10^1	10^4	1130.4	1.3043	0.94942	1.1155
32	10^5	1	10^2	10^{-2}	683.96	6.3854	1.8081	1.3059
33	10^6	1	25	0.04	752.90	9.2986	1.9363	1.1893
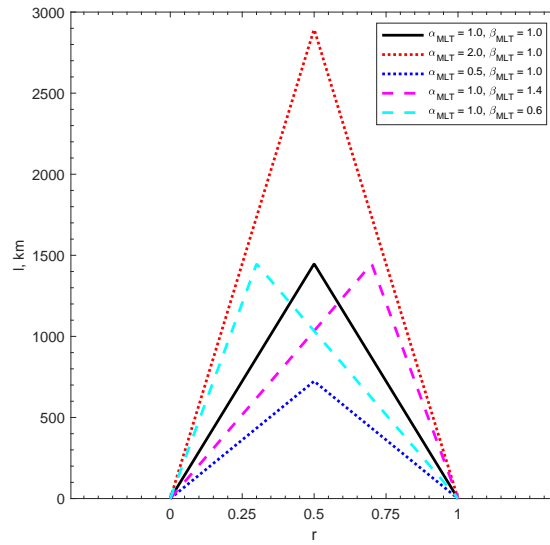
Figure 1. Distributions of mixing length for different combinations of the calibration parameters α_{MLT} and β_{MLT}.
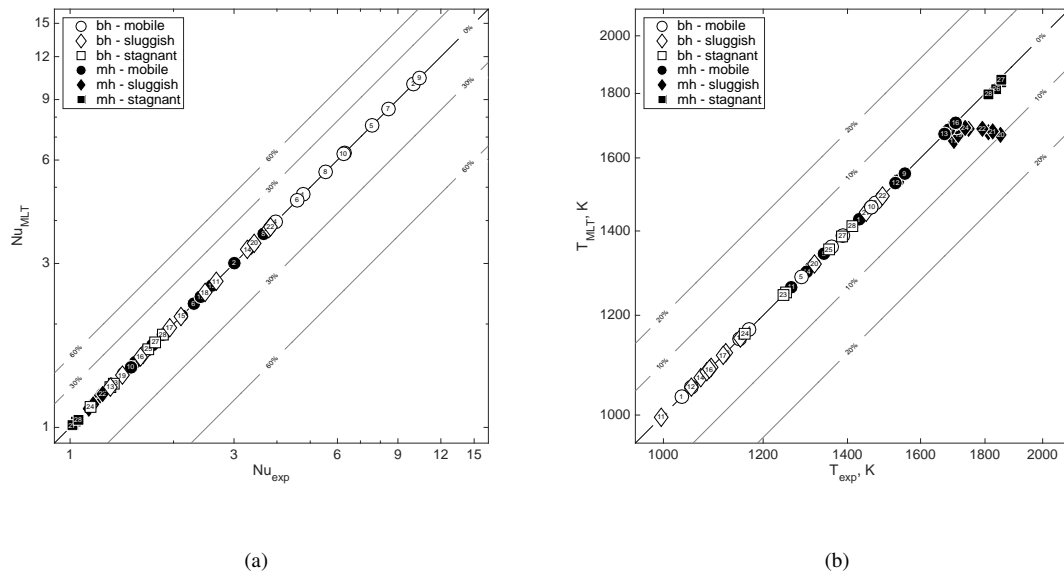
(a)

(b)
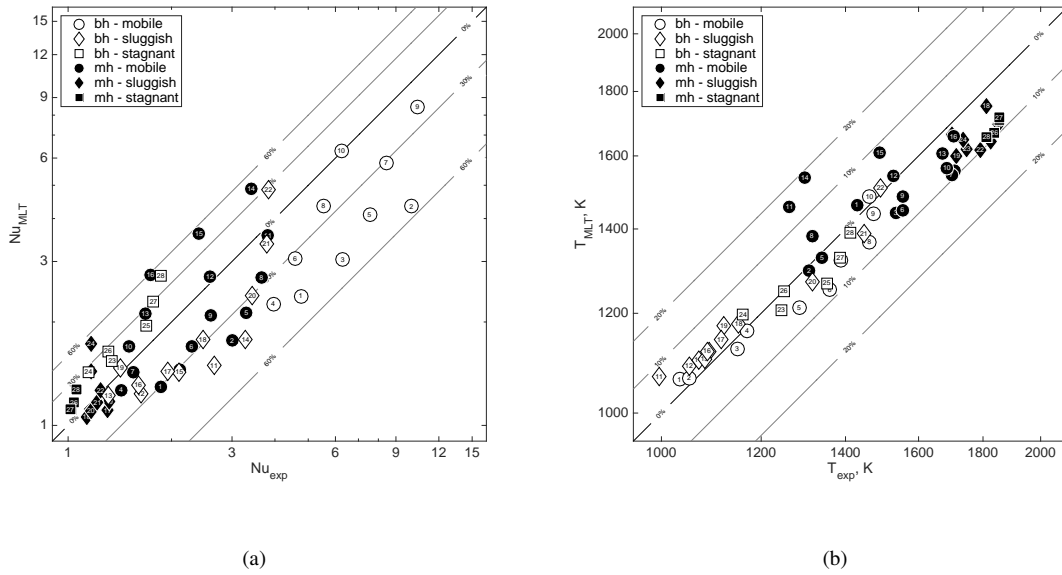
Figure 2. Comparison of (a) non-dimensional heat fluxes and (b) average temperatures. Calculations according to the conventional mixing-length theory are compared to the results of the numerical simulation experiments compiled in Tab. 2. The numbers inside each symbol refer to the simulation case. Bottom-heated cases are shown by white symbols, while mixed-heated cases by black symbols.

(a)

(b)
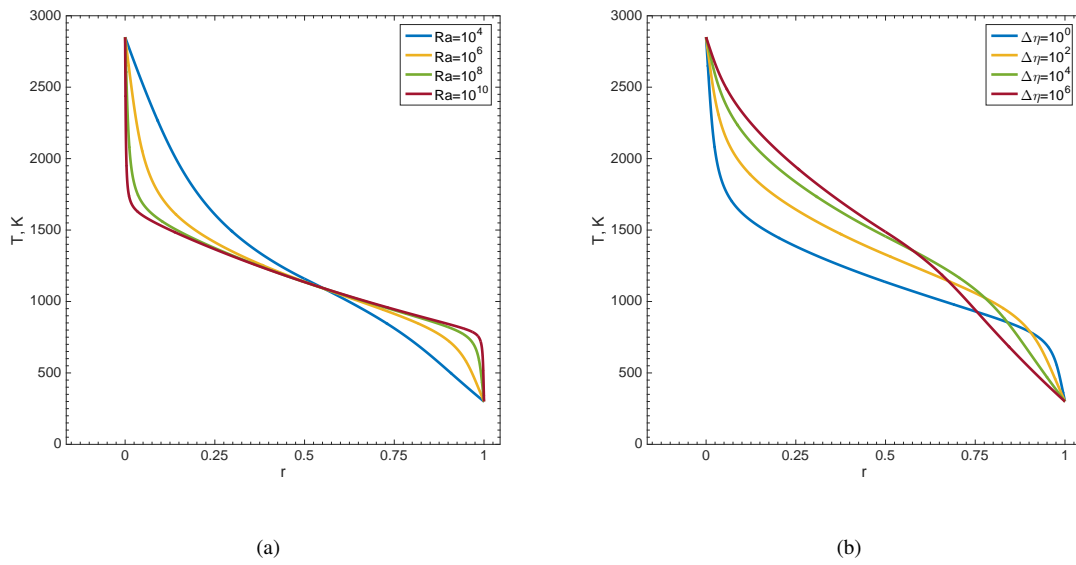
Figure 3. Distributions of temperature for fluids heated from below: (a) isoviscous case ($\Delta\eta = 10^0$) and different Rayleigh numbers; (b) fixed Rayleigh number Ra of 10^7 and different viscosity contrasts. Note that the distance to the nearest thermal boundary layer (conventional MLT) has been taken as local mixing length during all calculations.
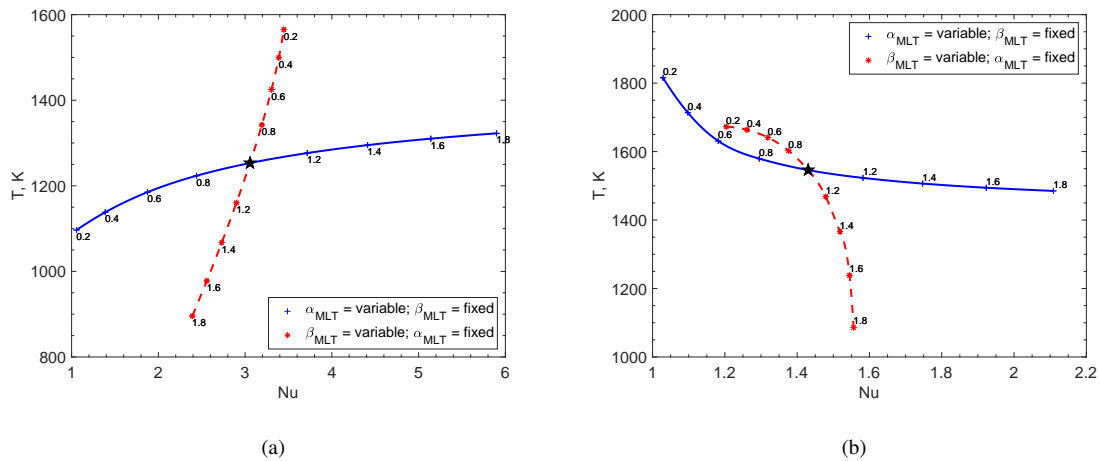
Figure 4. Effect of the calibration parameters α_{MLT} and β_{MLT} on Nusselt number and average temperature for (a) bottom heating and (b) mixed-mode heating. By default, fixed means that the calibration parameter is set to 1. Note that a Rayleigh number Ra of 10^7 and a viscosity contrast $\Delta\eta$ of 10^3 have been chosen for the calculations.

(a)   (b)

Figure 5. Comparison of (a) non-dimensional heat fluxes and (b) average temperatures. Calculations according to the calibrated mixing-length theory are compared to the results of the numerical simulation experiments complied in Tab. 2. The numbers inside each symbol refer to the simulation case. Bottom-heated cases are shown by white symbols, while mixed-heated cases by black symbols.
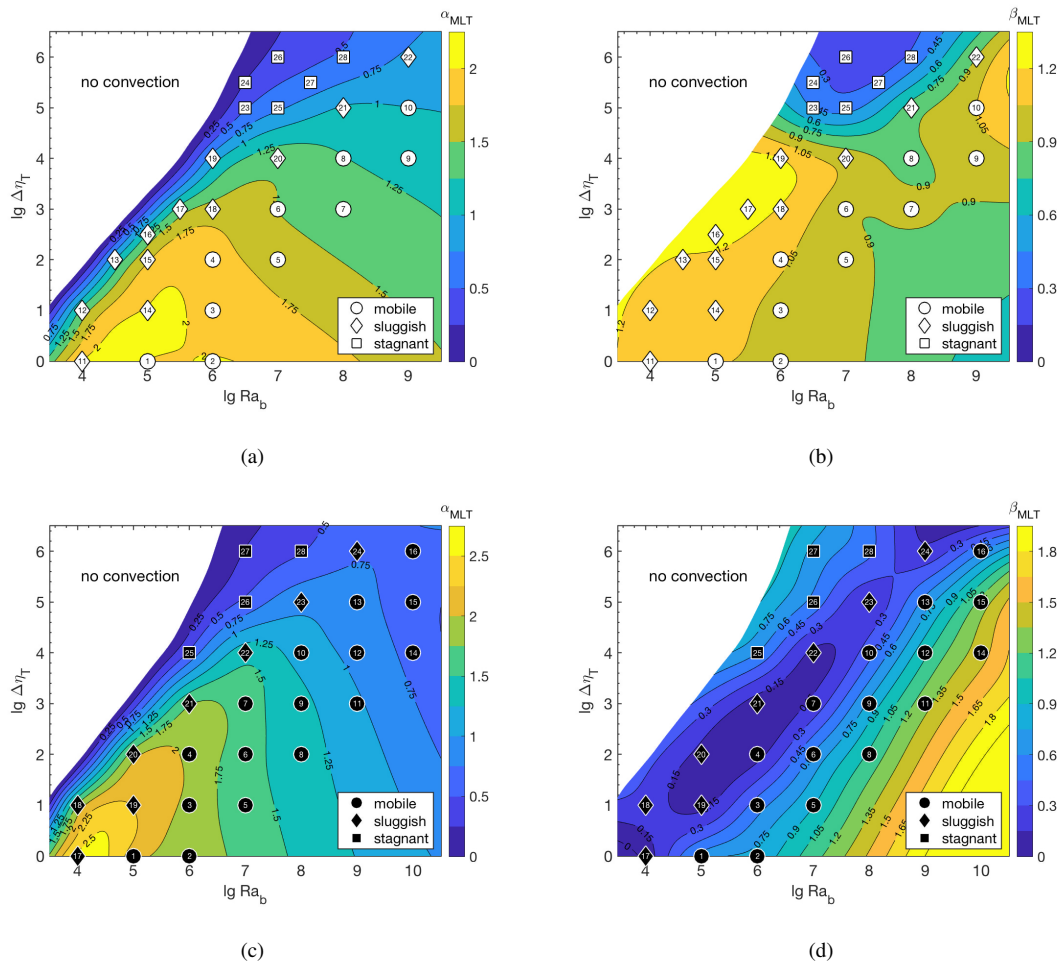
Figure 6. Mixing-length calibration parameters α_{MLT} and β_{MLT} for (a) and (b) bottom heating and (c) and (d) mixed-mode heating. The numbers inside each symbol refer to the simulation case. The different symbols correspond with a certain range of Péclet numbers and group each dataset into major convective regimes.
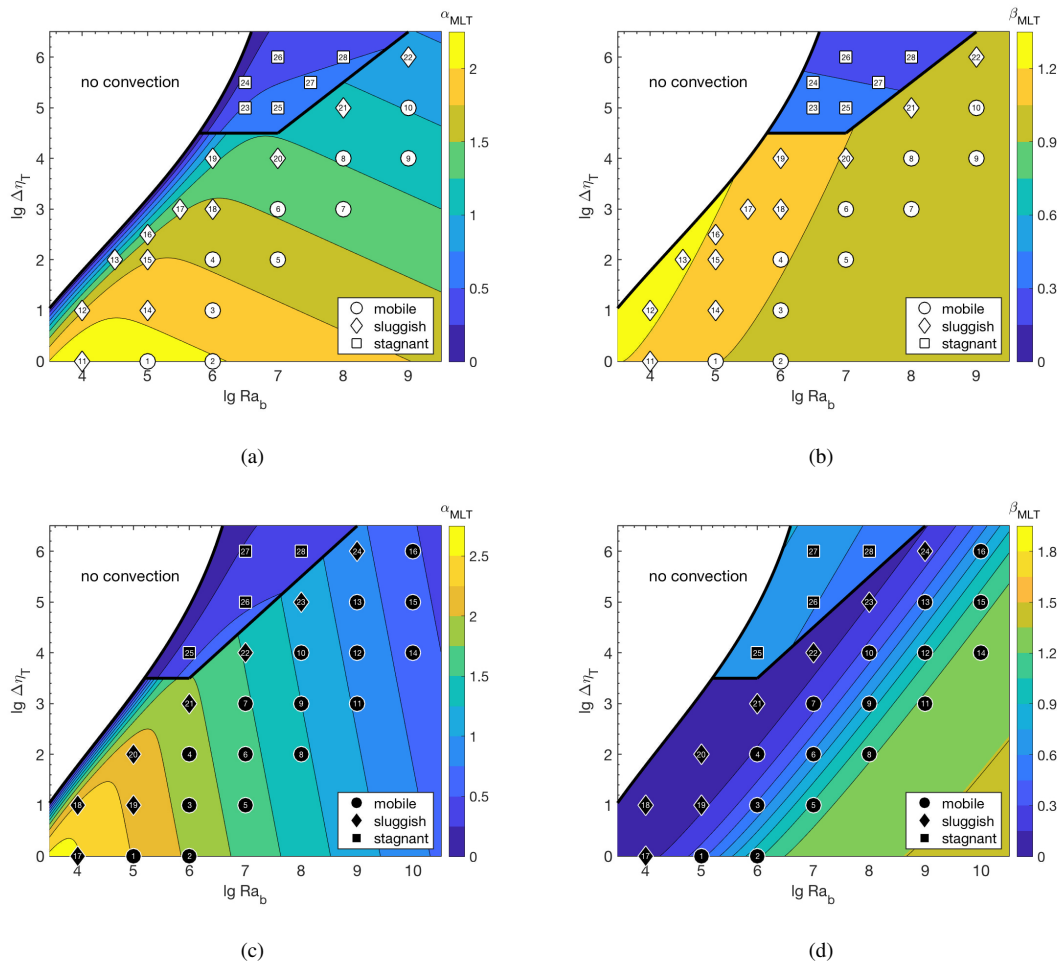
Figure 7. Same as Fig. 6, however the maps have been obtained from the regression model by assuming a major discontinuity between transitional and conductive-lid convection (thick black boundary line). The shape of the sharp boundary itself has been chosen arbitrarily to fit between points.
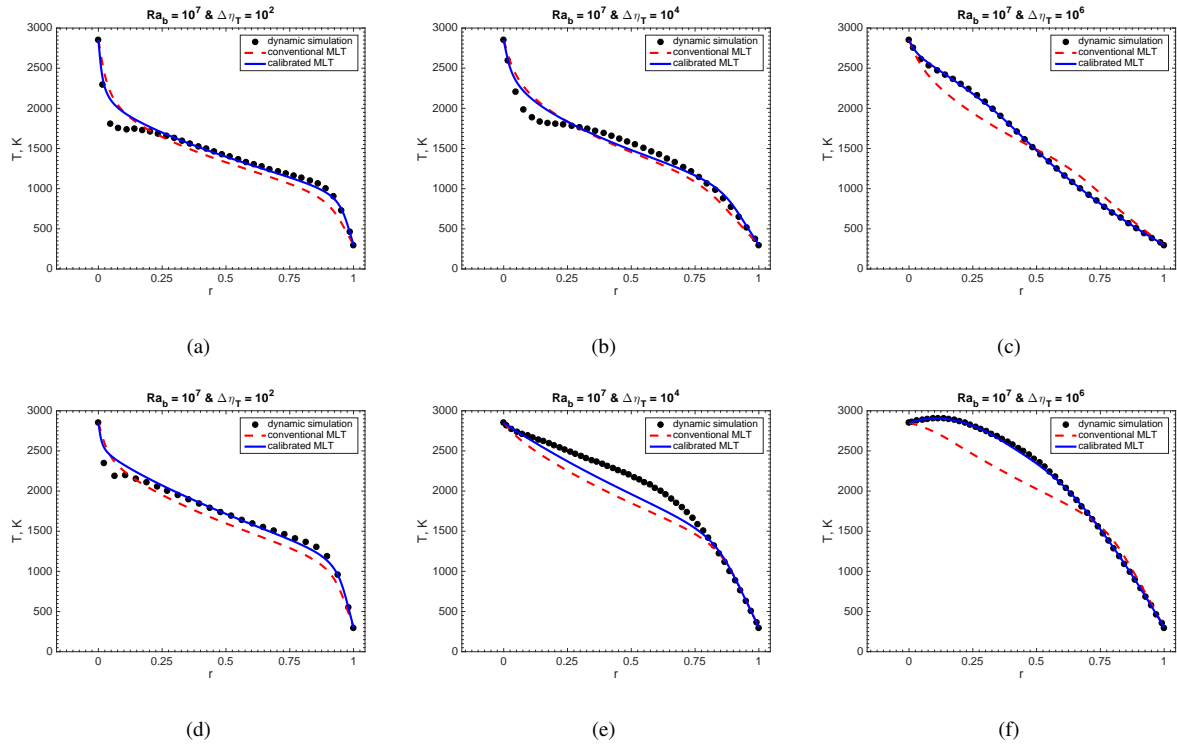
Figure 8. Temperature distribution according to our fully dynamic simulations compared to results from the conventional and the calibrated mixing-length theory, respectively. While panels in the first row show bottom-heated cases, panels in the second row correspond to cases employing mixed-mode heating. The first, second, and third columns show mobile-lid, sluggish-lid, and stagnant-lid cases, respectively.
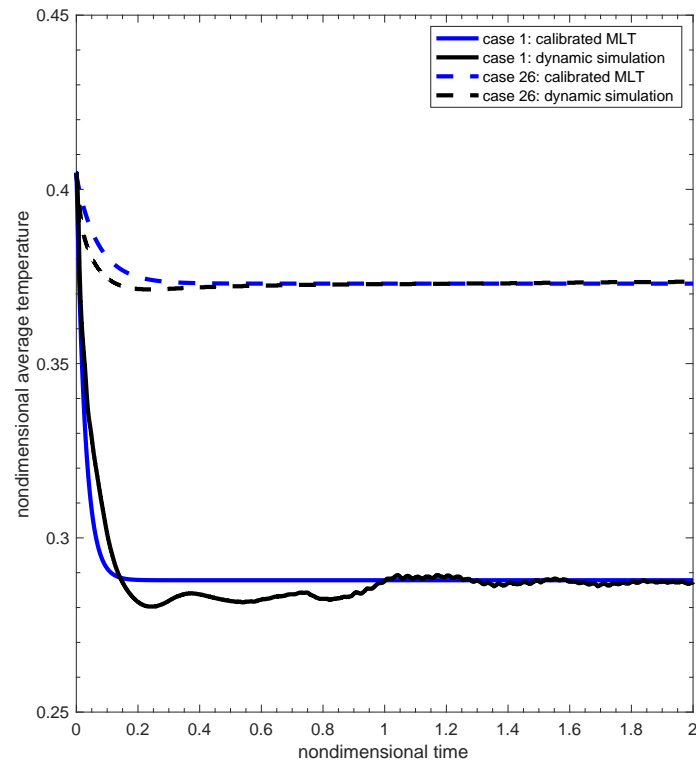
Figure 9. Comparison between the time dependence of the average mantle temperature obtained in the direct 3-D simulations and using the calibrated mixing length.